

# Precise Analysis of Microstructural Effects on Mechanical Properties of Cast ADC12 Aluminum Alloy

MITSUHIRO OKAYASU, SHUHEI TAKEUCHI, MASAKI YAMAMOTO,  
HIROAKI OHFUJI, and TOSHIHIRO OCHI

The effects of microstructural characteristics (secondary dendrite arm spacing, SDAS) and Si- and Fe-based eutectic structures on the mechanical properties and failure behavior of an Al-Si-Cu alloy are investigated. Cast Al alloy samples are produced using a special continuous-casting technique with which it is easy to control both the sizes of microstructures and the direction of crystal orientation. Dendrite cells appear to grow in the casting direction. There are linear correlations between SDAS and tensile properties (ultimate tensile strength  $\sigma_{UTS}$ , 0.2 pct proof strength  $\sigma_{0.2}$ , and fracture strain  $\epsilon_f$ ). These linear correlations, however, break down, especially for  $\sigma_{UTS}$  vs SDAS and  $\epsilon_f$  vs SDAS, as the eutectic structures become more than 3  $\mu\text{m}$  in diameter, when the strength and ductility ( $\sigma_{UTS}$  and  $\epsilon_f$ ) decrease significantly. For eutectic structures larger than 3  $\mu\text{m}$ , failure is dominated by the brittle eutectic phases, for which SDAS is no longer strongly correlated with  $\sigma_{UTS}$  and  $\epsilon_f$ . In contrast, a linear correlation is obtained between  $\sigma_{0.2}$  and SDAS, even for eutectic structures larger than 3  $\mu\text{m}$ , and the eutectic structure does not have a strong effect on yield behavior. This is because failure in the eutectic phases occurs just before final fracture. *In situ* failure observation during tensile testing is performed using microstructural and lattice characteristics. From the experimental results obtained, models of failure during tensile loading are proposed.

DOI: 10.1007/s11661-015-2747-1

© The Minerals, Metals & Materials Society and ASM International 2015

## I. INTRODUCTION

FOR environmental reasons, reductions in automotive exhaust gases, such as carbon dioxide and nitrogen oxides, are required. With this aim, automotive parts made of heavy steel have been replaced with lighter metals such as aluminum alloys. The Al-Si-Cu alloy family (ADC12) is widely employed in the automotive industry because of its good castability, high strength, and low density. In recent years, there has been increasing use of automotive parts made of cast Al alloy, a number of which are produced by high-pressure and high-speed casting, *i.e.*, die casting. High-pressure die-casting technology has the advantage of providing good mechanical properties because of the high cooling rate used in the process.<sup>[1]</sup> However, die-cast ADC12 components possess complicated microstructures and exhibit various defects, making them unsuitable for the automotive industry, and the use of cast ADC12 alloys to replace steel in the manufacture of safety-critical

parts in automobiles has been considerably restricted because of their lower strength and lower ductility.

From our previous work, it appears that failure in cast ADC12 alloys is strongly influenced by  $\alpha$ -Al grains (through their effect on secondary dendrite arm spacing, SDAS), eutectic phases, crystal orientation, and casting defects. Mechanical properties of high-pressure die-cast ADC12 alloy have been investigated, and it has been found that failure (or crack initiation) occurred from casting defects, for example, cold flakes and porosity.<sup>[2,3]</sup> There are various casting defects in die-cast ADC12 alloys, such as porosities, shrinkage cavities, oxide layers, and cold flakes.<sup>[2,3]</sup> Zhao *et al.*<sup>[4]</sup> have investigated the tensile properties of ADC12 die-cast plate samples, which are directly influenced by porosity and serrated faces. It has been reported by Jana *et al.*<sup>[5]</sup> that fatigue cracks in cast Al alloy emanate from the edges of porosities as a result of the high stress concentration there. Mechanical properties are also affected by microstructural characteristics, such as  $\alpha$ -Al grains and eutectic phases. Many investigators have found that SDAS is a significant factor determining the mechanical properties of cast Al alloys, with smaller SDAS leading to better mechanical properties, *i.e.*, grain-boundary strengthening. It is also considered that high mechanical properties could be obtained in the Al alloys with smaller SDAS due to the decrement of porosity.<sup>[6]</sup> Youssef *et al.*<sup>[7]</sup> synthesized a bulk nanocrystalline Al-Mg alloy that possessed the excellent strength of Al-5083 alloy along with good ductility. Good mechanical properties are achieved in cast Al alloys by  $\alpha$ -Al grain refinement, *i.e.*, a submicrometer grain size is a

---

MITSUHIRO OKAYASU, Associate Professor, SHUHEI TAKEUCHI, Ph.D. Candidate, and MASAKI YAMAMOTO, Undergraduate Student, are with the Department of Materials Science and Engineering, Ehime University, 3 Bunkyo-cho, Matsuyama, Ehime, 790-8577, Japan. Contact e-mail: mitsuhiro.okayasu@utoronto.ca  
HIROAKI OHFUJI, Associate Professor, is with the Geodynamics Research Center, Ehime University, 2-5 Bunkyo-cho. TOSHIHIRO OCHI, Director, is with the Ochi Foundry Inc., 1016 Tanouuwagata Tanbara-cho, Saijo, Ehime, 791-0522, Japan.

Manuscript submitted June 2, 2014.

Article published online 19 January 2015

significant advantage,<sup>[8]</sup> although, for most metals, very small grains (10 nm) result in poorer mechanical properties because of an inability to support dislocation pile-ups.<sup>[9]</sup> Furthermore, the effect of eutectic structure (size and shape) on mechanical properties has been considered for cast Al alloys, and it appears that large and elongated eutectic particles (Fe-based phase) result in lower mechanical strength.<sup>[10]</sup> The crack propagation rate in Al-Si-Mg alloy varies because of the agglomerated Si particles in the eutectic region; moreover, cracks in the  $\alpha$ -Al grains propagate rapidly in comparison with cracks growing in the eutectic and in grain boundaries.<sup>[11]</sup> Interesting work has been carried out by Wang,<sup>[12]</sup> where the tensile properties and fracture characteristic of cast Al alloys are dependent on not only SDAS but also size and shape of eutectic Si particles and Fe-rich intermetallic. Wang<sup>[13]</sup> has also reported the plastic deformation behavior of the cast Al alloys: at low strain region, the aspect ratio of the eutectic particles and matrix strength are attributed to the work hardening, whereas at large strain region, the hardening rate depends on SDAS. In our previous studies, it was shown that the crystal orientation of cast Al alloys is one of the important factors determining tensile properties, with uniform crystal formation in cast Al alloys possessing high ductility.

From the above literature survey, it is obvious that the mechanical properties of cast ADC12 alloys are sensitive to their microstructural characteristics.<sup>[14]</sup> However, the significance of microstructure in determining mechanical properties has not been clearly reported—for example, which microstructural characteristics ( $\alpha$ -Al grains or eutectic phases) have the more significant effect on mechanical properties? In the present work, an attempt is made to clarify the influences of microstructures, such as  $\alpha$ -Al phases and Fe- and Si-based eutectic phases, on the mechanical properties of cast Al alloys.

## II. EXPERIMENTAL PROCEDURES

In the present work, a JIS-ADC12 Al alloy was used. This alloy is used in various automotive parts, such as transmission cases, converter housings, and engine blocks. The main chemical composition of ADC12 is (mass pct) 10.6Si, 2.5Cu, 0.3Mg, 0.5Zn, 1.1Fe, 0.3Mn, and 0.1Ni, with the remainder consisting of Al. The ADC12 samples were prepared by the heated-mold continuous-casting (HMC) process. The HMC process was used because it produces high-quality cast samples without casting defects. In addition, this casting method allows easy control of both microstructure size<sup>[15]</sup> and crystal orientation.<sup>[16]</sup> On the basis of the material characteristics, microstructural effects on mechanical properties of cast Al alloys can be determined accurately. Before the casting process, a molten metal treatment was conducted with a flux based on K-Cl-F-Al to remove inclusions and oxide. Figure 1 shows a schematic illustration of a horizontal-type HMC arrangement, consisting of a melting furnace, a heated graphite mold 5 mm in diameter, a graphite crucible, a cooling device, and a dummy rod for withdrawal of the cast sample. About 0.2 kg of ADC12 ingot was placed in the graphite crucible for melting, with the graphite mold heated to approximately 898 K (625 °C), which is just above the liquidus of the ADC12 alloy. The melted Al alloy in the crucible was fed continuously into the mold through a runner. Details of the HMC process can be found in References 15 through 17. To obtain various microstructural characteristics, the casting operation was carried out at different speeds, from 0.1 to 7.5 mm/s. With our HMC process, round rod samples 5 mm in diameter and 1 m in length were produced. It should be pointed out first that, in the previous work, excellent mechanical properties of the HMC-ADC12 samples were found,<sup>[16,18]</sup> but those samples were made only at 1.9 mm/s.

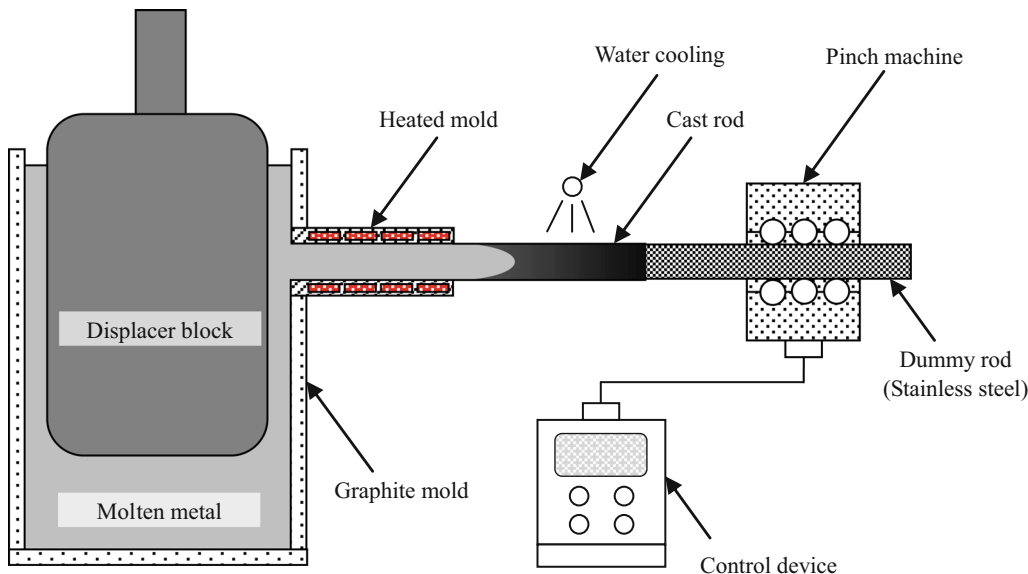


Fig. 1—Schematic illustration of the horizontal-type heated continuous-casting device.

Tensile and fatigue properties were investigated at room temperature using an electro-servo-hydraulic system with 50-kN capacity. Dumbbell-shaped round specimens (diameter 2 mm and length 4 mm) were employed. The tensile properties were evaluated *via* curves of tensile stress *vs* tensile strain, which were monitored during the tensile tests using a data acquisition system in conjunction with a computer through a standard load cell and strain gage. The test was conducted at a speed of 1 mm/min until the specimen fractured completely. The fatigue properties were evaluated from the relationship between the stress amplitude and the number of cycles to failure (the  $S_a$ - $N_f$  curve). The fatigue tests were carried out with cyclic loading at a frequency of 30 Hz and a load ratio of 0.1 until  $10^7$  cycles or complete fracture of the sample.

To further understand the mechanical properties of the cast Al alloy in details, the hardness measurement was carried out using a micro-Vickers hardness tester (HM-112 Akashi) with the indentation load of 9.8 N for 15 seconds. The sample surfaces were polished to mirror level before the hardness measurement.

The microstructural characteristics of the ADC12 alloys were examined using optical microscopy, energy-dispersive X-ray spectroscopy (EDX), and electron backscatter diffraction (EBSD). For EDX, a JSM-6510 scanning electron microscope was employed, and the analysis was conducted with an acceleration voltage of 15 kV. For EBSD analysis, a JSM-7000F high-resolution electron microscope was used. The EBSD scans were performed with an acceleration voltage of 15 kV, a beam current of 5 nA and a step size of less than 20  $\mu\text{m}$ . To analyze the crystal orientation characteristics, HKL Channel 5 software was used. The EBSD analysis was performed on the cast samples in directions perpendicular and parallel to the casting direction.

### III. RESULTS

#### A. Microstructural Characteristics

Figure 2 shows optical micrographs and EDX analyses of HMC-ADC12 samples produced at various casting speeds. From these observations, it can be seen that the microstructures basically consist of needle-shaped eutectic phases of Si and Al-Fe-Si ( $\text{Al}_8\text{SiFe}_2$ ),<sup>[16,19]</sup> embedded between primary  $\alpha$ -Al grains. Because of the acicular nature of the Si- and Fe-based eutectic particles in the interdendritic regions,<sup>[5]</sup> these particles cause a high stress concentration when high stress is applied to the samples. It is clear from the optical micrographs that the  $\alpha$ -Al dendrite cells grow in the casting direction. Because of the different cooling rates (resulting from the different casting speeds), grain structure transition occurred, *i.e.*, equiaxed or columnar microstructure.<sup>[20]</sup> In this case, equiaxed grains can be seen in the cast samples created at low cooling rates (CR), while columnar structures are seen for the high CR ones. The sizes of the  $\alpha$ -Al grains and the eutectic structures also differ among the samples, because of the different casting speeds. In this case, high cooling rate is

required to make the cast samples at the high casting speeds as the melt Al alloy cannot be solidified to the round rod of 5 mm in diameter, *i.e.*, about 1064 K/s (at 7.5 mm/s), which estimated by  $\text{CR} = 2 \times 10^4 \text{SDAS}^{-2.67}$ .<sup>[18]</sup> The measurement data ( $n = 50$ ) are plotted in Figure 3, where it can be seen that the higher the cooling rate, the finer is the microstructure. The mean SDAS was 3.0  $\mu\text{m}$  for the high casting speed of 7.5 mm/s and 22.0  $\mu\text{m}$  for the low speed of 0.1 mm/s. On the other hand, the mean diameters of the eutectic structures for the high (7.5 mm/s) and low (0.1 mm/s) casting speeds were 0.4 and 10.0  $\mu\text{m}$ , respectively. It should be pointed out that, from our microstructural observations, no clear cast defects (pores or inclusions) were detected in any of the cast samples.

Figure 4 depicts crystal orientation (inverse pole figure, IPF) maps of the cast samples obtained by EBSD. The color level of each pixel in the IPF map is determined according to the deviation of the measured orientation, as indicated in the stereographic projection. The black solid lines show misorientation angles of more than 5 deg, which define the grain boundaries. In Figure 4(a), the observation was conducted in the direction perpendicular to the casting direction, and a relatively uniform lattice orientation can be seen over a large area in almost all the samples. In our samples, the crystal orientation of the HMC samples is almost perfectly orientated with  $\langle 100 \rangle$ , which formed perpendicular to the casting direction, as seen in the pole figure (Figure 4(a)). The uniformly organized crystal formation in the HMC samples is due to the unidirectional solidification process.

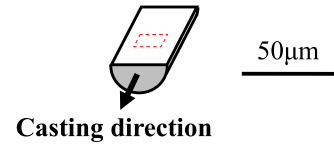
Figure 4(b) shows IPF maps for the representative cast samples (0.1, 3.5, and 7.5 mm/s) observed in the direction parallel to the casting direction. In contrast to the crystal orientation on the surface perpendicular to the casting direction, the orientation on the surface parallel to the casting direction varies among the samples. This is due to the different polishing directions on the basis of the (100) planes. It is interesting to note that stripe-shaped grain boundaries are seen on the face parallel to the casting direction. This can be attributed to the unidirectional grain growth. The distance between the grain boundaries becomes narrower with increasing cooling rate (Figure 4(b)). This trend is related to the size of the microstructures as shown in Figure 3. Such grain boundaries could result in different mechanical properties.

#### B. Mechanical Properties

Figure 5 shows the variation of the Vickers hardness (HV) as a function of casting speed. As seen, the hardness value increases nonlinearly with increasing casting speed. It should be pointed out that the hardness values in Figure 5 are widely scattered, especially for the samples produced at low casting speeds (*i.e.*, less than 0.4 mm/s), in which the low-hardness data are dominated by the hardness of the soft  $\alpha$ -Al grains, and the high-hardness data can be attributed to the greatly enlarged hard eutectic structures. In fact, the Martens hardness (HM) of  $\alpha$ -Al grains, examined by a special

(a) Optical micrographs

ADC12-HMC samples				
0.1 mm/s	0.4 mm/s	0.8 mm/s	1.9 mm/s	2.7 mm/s
SDAS: 22.0 μm	SDAS: 18.2 μm	SDAS: 11.9 μm	SDAS: 7.3 μm	SDAS: 6.0 μm
3.5 mm/s	4.5 mm/s	5.5 mm/s	6.5 mm/s	7.5 mm/s
SDAS: 5.6 μm	SDAS: 5.4 μm	SDAS: 5.1 μm	SDAS: 3.8 μm	SDAS: 3.0 μm



(b) EDX analyses of the HMC samples

	SEM image	Al-Kα	Si-Kα	Cu-Kα	Fe-Kα
0.1 mm/s					
3.5 mm/s					
7.5 mm/s					

Fig. 2—(a) Optical micrographs and (b) EDX analyses of the cast samples, showing the microstructural characteristics of cast ADC12 Al alloys.

nano-indentation hardness test machine, is about 798 MPa, which is about five times and eight times lower than the values for eutectic Si and the Al-x-Fe base structure, respectively.<sup>[21]</sup>

Figure 6 shows the representative tensile stress vs strain curves for each cast sample. As can be seen, the behavior of the tensile properties differs among the samples. On the basis of these stress-strain curves, the tensile properties were investigated further.

Figure 7 shows the variations of ultimate tensile strength  $\sigma_{UTS}$ , 0.2 pct proof strength  $\sigma_{0.2}$  and fracture strain  $\epsilon_f$  as functions of casting speed. It can be seen in Figure 7(a) that like the results for Vickers hardness, the mean ultimate tensile strength increases nonlinearly with increasing casting speed, with changing slope severely at a casting speed between 1 and 3 mm/s. The mean maximum  $\sigma_{UTS}$  is approximately 400 MPa for the samples produced at the highest casting speed of

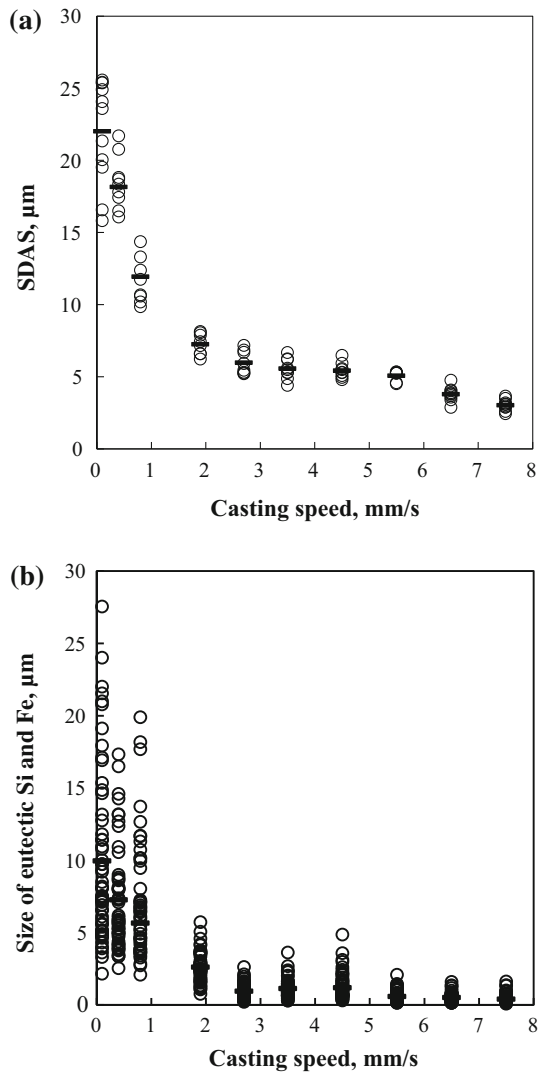


Fig. 3—(a) Secondary dendrite arm spacing (SDAS) and (b) sizes of Si- and Fe-based eutectic particles in cast ADC12 Al alloys.

7.5 mm/s, which is about 70 pct higher than for the samples produced at 0.1 mm/s. Such a high tensile strength can be simply explained by the presence of very fine microstructures in these samples. It should be noted that the overall tensile strength of the HMC samples is much higher (more than 1.5 times) than that of ADC12 alloys produced by conventional die-casting and gravity-casting processes.<sup>[16,22]</sup> Tensile properties of the high-pressure die-cast ADC12 with T6 and T7 treatments were carried out, and it appears that their ultimate tensile strengths are around 350 MPa,<sup>[23]</sup> which is still lower than that for our highest  $\sigma_{UTS}$ . Moreover, another approach was executed to obtain excellent tensile properties, in which ADC12 alloy was produced by the following process<sup>[24]</sup>: (i) rapidly solidified ADC12 alloy was cold rolled before degassing, (ii) the ADC12 sample was machined with hot extrusion process at 673 K (400 °C), and (iii) the machined sample was heat treated (T6). The tensile properties of the ADC12 sample increase, which is slightly higher than that for our highest  $\sigma_{UTS}$ . In order to verify this, the tensile

properties of our ADC12 samples after T6 treatment were investigated, where cast sample created at cooling speed of 1.9 m/s was used. In this case, artificial aging process was conducted to and held at 433 K (160 °C) for 13 hours following solution treatment: 773 K (500 °C) for 10 hours in air furnace followed by water quenching. The tensile properties increase apparently after the T6 treatment ( $\sigma_{UTS} = 380$  MPa and  $\epsilon_f = 10$  pct), which are closed to those for the as-cast ADC12 at 7.5 m/s, see Figure 7.

As shown in Figure 7(b),  $\sigma_{0.2}$  increases linearly with increasing casting speed, which is possibly a consequence of the Hall–Petch relation. Interestingly, the variation of strain with casting speed has a convex shape, as shown in Figure 7(c), although the data plots are scattered: the strain increases with increasing casting speed until about 3.5 mm/s and then decreases when the speed is further increased. This behavior, particularly for the samples created at lower casting speeds, is in contrast to the normal inverse relationship between strain and strength (*i.e.*, the higher the strength, the lower the ductility). This may be a consequence of the complicated multiple microstructures of our samples. To understand this inconsistency, the effects of grain size on tensile properties were investigated.

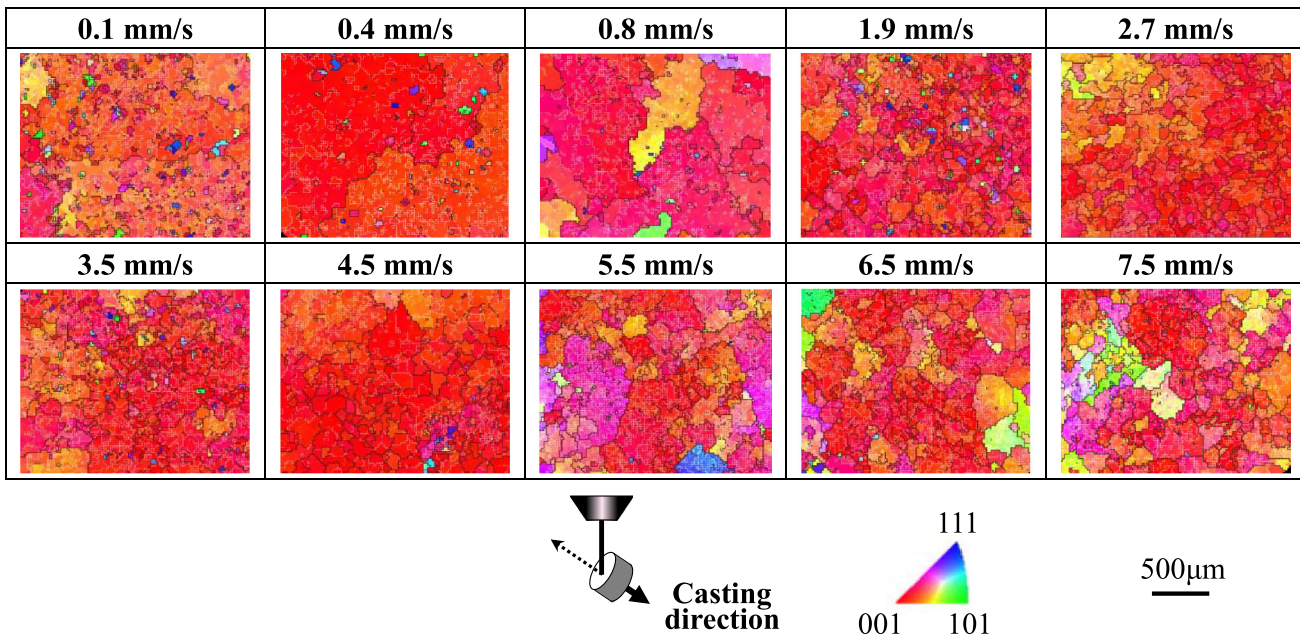
Figure 8 shows the relationship between the tensile properties ( $\sigma_{UTS}$ ,  $\sigma_{0.2}$  and  $\epsilon_f$ ) and the inverse square root of SDAS ( $SDAS^{-1/2}$ ). It should be pointed out that SDAS was employed as parameter in this approach although it is also considered to be the grain size instead of SDAS. The reason for SDAS selected is first that the  $\alpha$ -Al grains grow with dendrite formation clearly, and the effect of SDAS and grain size on mechanical properties is similarly obtained for the related aluminum alloy.<sup>[25]</sup> The results all show basically similar trends to those in Figure 7, with nonlinear and linear correlations being found for  $\sigma_{UTS}$  vs  $SDAS^{-1/2}$  and  $\sigma_{0.2}$  vs  $SDAS^{-1/2}$ , respectively, in Figure 8(a) and (b). Those relationships were caused by the fact that the SDAS is reflected by the cooling rate (CR). For the data analysis with the theory of grain-boundary dislocation sources, *i.e.*, the Hall–Petch relation, the SDAS was employed as data parameter in Figure 8. Although nonlinear correlation is obtained for our  $\sigma_{UTS}$  vs  $SDAS^{-1/2}$ , linear relations were also reported in the previous works.<sup>[25,26]</sup> Moreover, some data seem to be scattered in  $\sigma_y$  vs SDAS.<sup>[27]</sup> Note that our data in Figure 8(a) may not be enough number to determine the nonlinear correlation, so further approach will be required in the future.

The relationship between  $\sigma_{0.2}$  and  $SDAS^{-1/2}$  may be explained in terms of grain-boundary strength, and is represented by the following equation:

$$\sigma_{0.2} = 59.0 \times SDAS^{-1/2} + 120.3, \quad [1]$$

with  $\sigma_{0.2}$  in MPa and SDAS in  $\mu\text{m}$ . As mentioned, almost linear  $\sigma_{0.2}$  vs  $SDAS^{-1/2}$  can be obtained. In the previous work, the microstructural effect on flow stress was introduced for cast aluminum A356 with fine and coarse grains, *e.g.*,  $SDAS = 20$  to  $30 \mu\text{m}$  and  $80$  to  $100 \mu\text{m}$ , where the higher flow stress is obtained for the Al alloy with coarse grains.<sup>[28]</sup> On the other hand, no

(a) Perpendicular to the casting direction



(b) Parallel to the casting direction

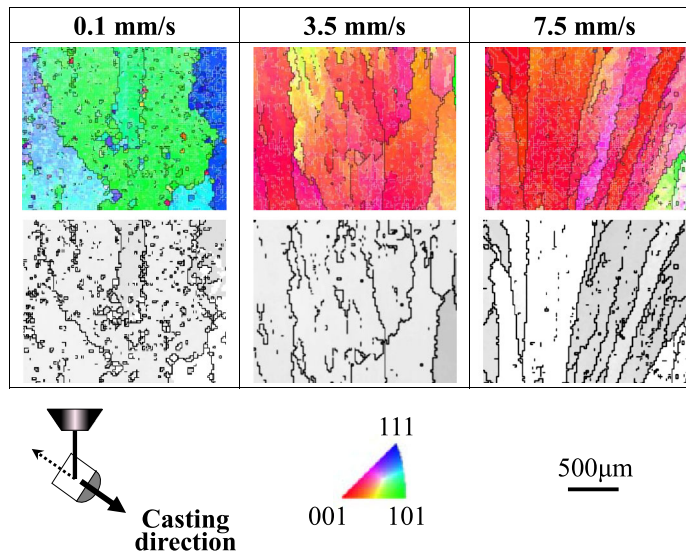


Fig. 4—Crystal orientation maps of cast ADC12 Al alloys observed in directions (a) perpendicular and (b) parallel to the casting direction.

clear correlation between  $\sigma_{0.2}$  and SDAS was obtained for the heat-treated cast Al alloy A356.<sup>[29]</sup> In the study by Youssef *et al.*,<sup>[7]</sup> the Hall–Petch approach was adopted and several Al alloys (nanocrystalline and polycrystalline) were employed. Using Eq. [1], the 0.2 pct proof strength has been estimated for two of these alloys: (i) nanocrystalline (nc) Al-5083 with grain size  $0.030 \mu\text{m}$  and (ii) polycrystalline (pc) Al-5083 with grain size  $55 \mu\text{m}$ .<sup>[7]</sup> The  $\sigma_{0.2}$  values thus obtained are 460.9 MPa for nc Al-5083 and 128.3 MPa for pc Al-5083. The estimated value of  $\sigma_{0.2}$  for the pc Al alloy is in good agreement with the experimental value of 145 MPa found by Youssef *et al.* In contrast, there is poor agreement between estimates (460.9 MPa) and

experiments (690 MPa) for the nc Al alloy (about 50 pct difference), which may be a consequence of the difference in grain size, which was of the order of nanometers for the alloys studied by Youssef *et al.* and micrometers for those in the present investigation, on which Eq. [1] is based. It should be pointed out that a convex  $\sigma_{0.2}$  variation in Al-Zn-Mg alloys has been reported by Kovács *et al.*,<sup>[30]</sup> who investigated the variation of  $\sigma_{0.2}$  with the diameter of precipitated particles. In their study, the yield strength is attributed to two different precipitated particle systems: the GP zone and the Orowan mechanism. In this instance, the largest yield stress is expected at an average radius of about 3 nm. The yield strength decreases, however, with increasing

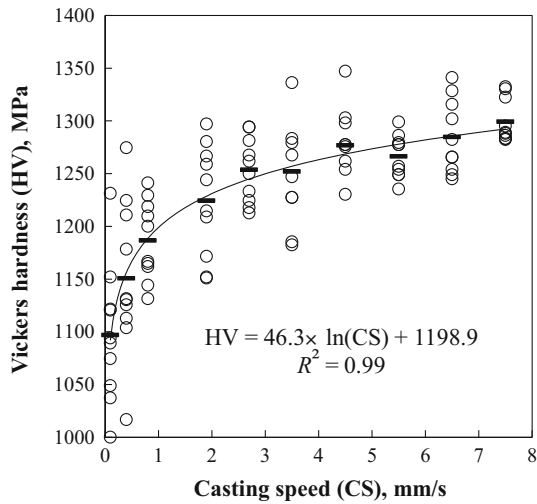


Fig. 5—Variation of Vickers hardness as a function of casting speed for cast ADC12 Al alloys.

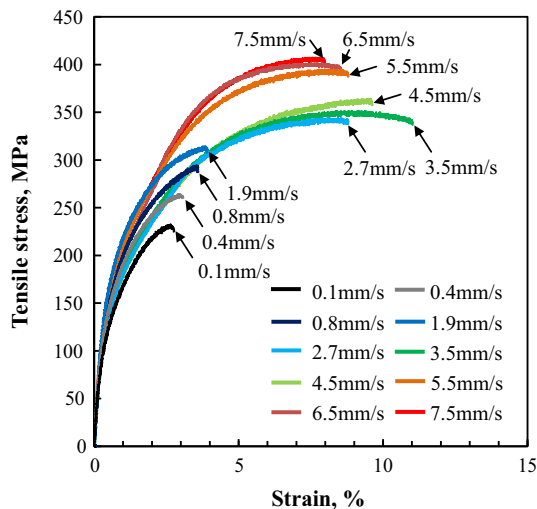


Fig. 6—Representative curves of tensile stress vs tensile strain for cast ADC12 Al alloys.

particle size of the  $\eta'$  phases (the Orowan mechanism). This is because of the wide range of particle sizes, including large particles. Kovács *et al.*, reported a clear convex strain variation in the  $\epsilon_f$ -SDAS relation, where  $\epsilon_f$  increases with increasing SDAS<sup>-1/2</sup> until SDAS<sup>-1/2</sup> = 0.4  $\mu\text{m}^{-1/2}$  and then decreases with further increases in SDAS<sup>-1/2</sup>. On the basis of the work in Reference 30 this convex behavior is related to the different microstructural characteristics. Tiryakioğlu *et al.*<sup>[31]</sup> have discussed the effects of SDAS on the ductility for various aluminum alloys, in which they have pointed out that “only a limited number of attempts have been made to explain the strong effect of SDAS on ductility from a micromechanical point of view.” They also introduced some related works, *e.g.*, an elongation increases with decreasing SDAS, and an increase in SDAS from 20 to 45  $\mu\text{m}$  would cause a drop in elongation from 11 to 5 pct. Even though the range of SDAS between 20 and

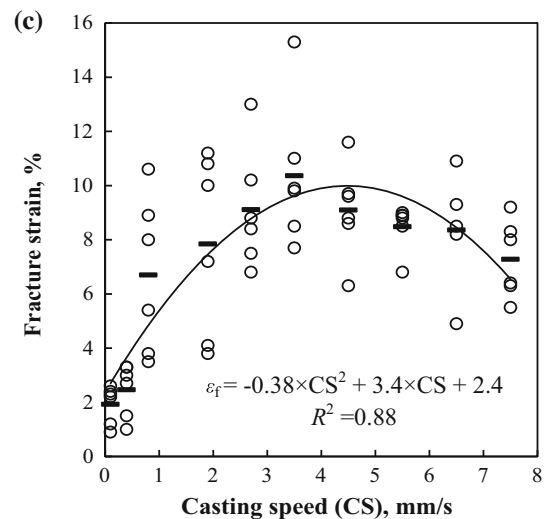
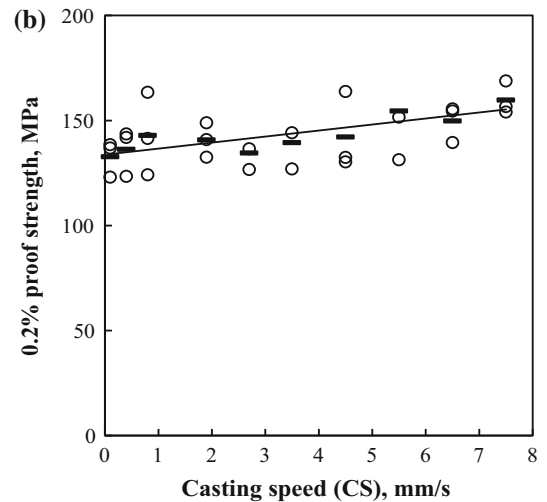
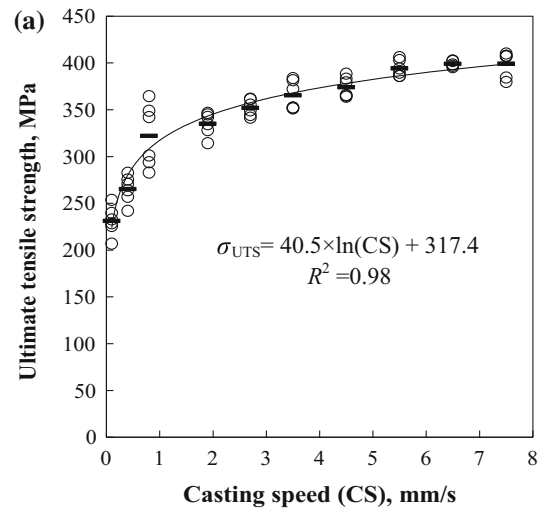


Fig. 7—Variation of tensile properties as functions of casting speed for cast ADC12 Al alloys: (a) ultimate tensile strength; (b) 0.2 pct proof strength; (c) fracture strain.

45  $\mu\text{m}$  is the large size compared to that for our Al alloy samples, the decrement of the elongation is similar trend of our experimental result shown in Figure 8(c). Because

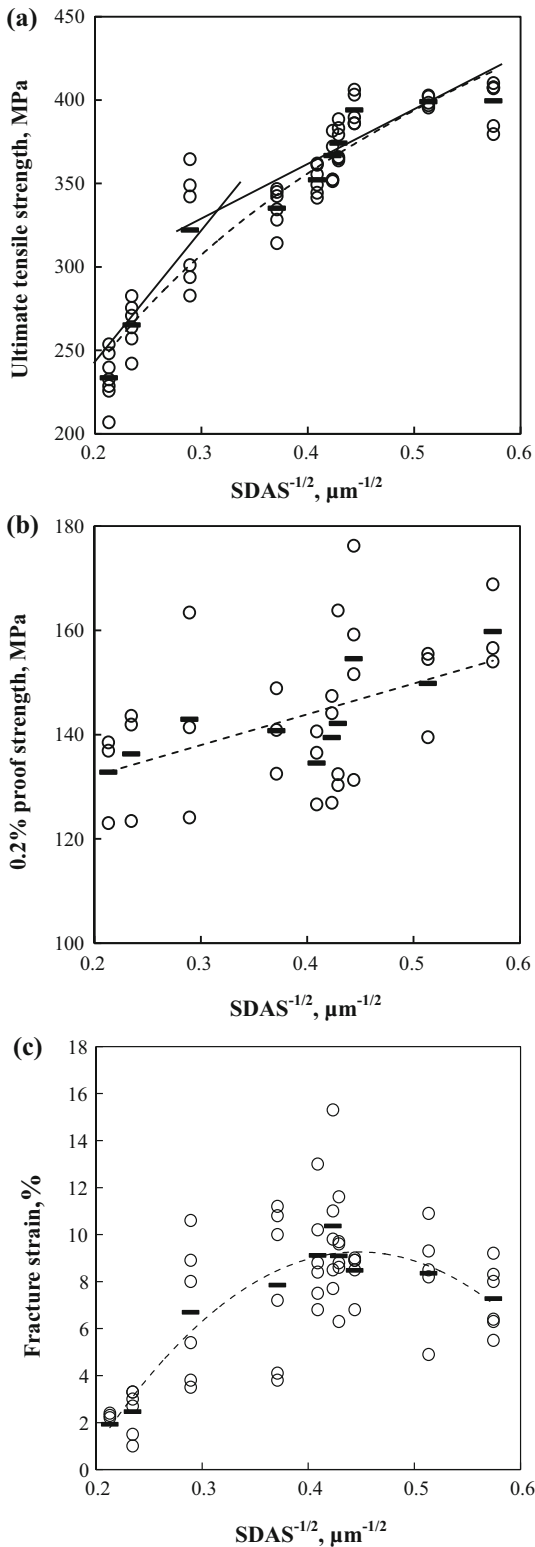


Fig. 8—Relationship between tensile properties and SDAS for cast ADC12 Al alloys: (a)  $\sigma_{\text{UTS}}$  vs  $\text{SDAS}^{-1/2}$ ; (b)  $\sigma_{0.2}$  vs  $\text{SDAS}^{-1/2}$ ; (c)  $\varepsilon_f$  vs  $\text{SDAS}^{-1/2}$ .

the crack growth occurs along the dendritic boundaries at the large SDAS,<sup>[31]</sup> the eutectic phases may be dominated feature to the ductility.

As mentioned previously, different microstructural characteristics were obtained, *e.g.*, equiaxed and columnar structure. Those structures could also be attributed to their mechanical properties. Eskin *et al.*<sup>[32]</sup> have introduced the related experimental results for the aluminum alloy, and the material ductility is different depending on the microstructural characteristics. In our samples, such structures (equiaxed and columnar) are related to the cooling rate although the cooling rate makes also the grain size as described. The authors believe that the mechanical properties are strongly attributed to the grain size, compared to the structural characteristics in this case, because the cooling rate is altered widely. However, further study will be required in the future.

It appears that hardness tests can be useful for the indirect determination of other mechanical properties, and studies of the relationship between hardness and tensile strength have been conducted by several investigators.<sup>[33,34]</sup> Figure 9(a) presents the relationship between the mean ultimate tensile strength and the mean hardness. As can be seen, there is linear correlation between  $\sigma_{\text{UTS}}$  and HV, with correlation rate  $R^2 = 0.96$ . On the other hand, the correlation rate between  $\sigma_{0.2}$  and hardness is as low as  $R^2 = 0.47$ . Tabor proposed the following formula to estimate the ultimate tensile strength (in MPa) from the diamond pyramid hardness<sup>[35]</sup>:

$$\sigma_{\text{UTS(Tabor)}} = \text{HV}/2.9 \times [1 - (m-2)] \times [12.5(m-2)/\{1 - (m-2)\}]^{m-2}, \quad [2]$$

where  $m$  is Meyer's hardness coefficient. Using Eq. [2], the ultimate tensile strengths of our samples were approximated, using our mean hardness data and taking  $m - 2 = 0.1$  as a first approximation.<sup>[35]</sup> The results are shown in Figure 9(b). There is a clear linear correlation between them ( $R^2 = 0.96$ ):

$$\sigma_{\text{UTS}} = 2.7\sigma_{\text{UTS(Tabor)}} - 707.5, \quad [3]$$

in MPa. However, in this case, the value of  $\sigma_{\text{UTS(Tabor)}}$  is not close to our experimentally obtained  $\sigma_{\text{UTS}}$ ; in other words, the coefficient in Eq. [3] is not close to 1. Thus, the Tabor model is not applicable for estimating the ultimate tensile strength of our Al alloy from its hardness.

Figure 10 shows the relationship between stress amplitude  $S_a$  and fatigue life  $N_f$  for representative samples produced at casting speeds of 0.1, 3.5, and 7.5 mm/s. In this case,  $10^7$  cycles are determined as the endurance limit, indicated by the arrows in Figure 10. It can be seen that the samples produced at 3.5 and 7.5 mm/s show the highest fatigue strengths and the samples produced at 0.1 mm/s the lowest. The  $S_a$ - $N_f$  curves for the samples produced at 7.5 and 3.5 mm/s almost coincide, although the fatigue strength for the 7.5 mm/s sample is slightly higher. The  $S_a$ - $N_f$  relationship is sometimes evaluated using the Basquin equation<sup>[5]</sup> as follows:

$$S_a = \sigma_f N_f^b, \quad [4]$$

in MPa, where  $\sigma_f$  is the fatigue strength coefficient and  $b$  is the fatigue exponent. The values of  $\sigma_f$  and  $b$  obtained



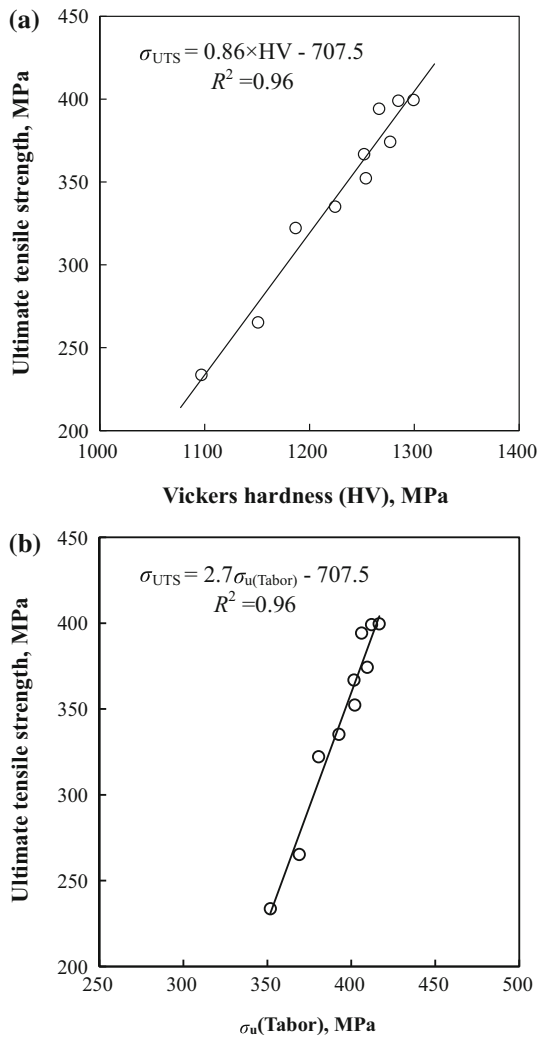


Fig. 9—(a) Relationship between  $\sigma_{UTS}$  and Vickers hardness and (b) Relationship between  $\sigma_{UTS}$  and  $\sigma_{u(Tabor)}$ .

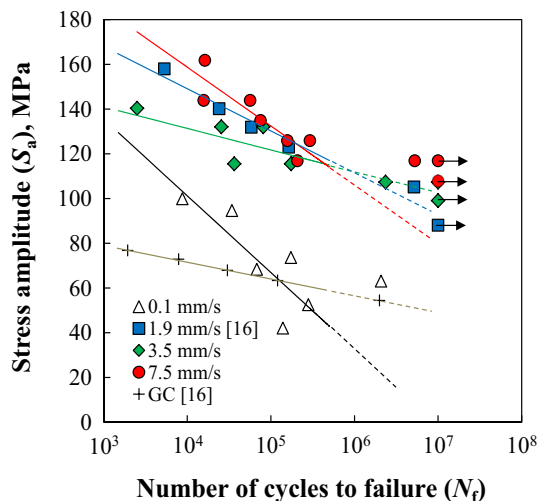


Fig. 10— $S_a-N_f$  curves for cast ADC12 Al alloys produced at casting speeds of 0.1, 3.5, and 7.5 mm/s.

using Eq. [4] for the three samples (0.1, 3.5, and 7.5 mm/s) are  $\sigma_f = 169.5, 179.7,$  and  $218.9$  MPa and  $b = -0.079, -0.034,$  and  $-0.042$ . Note, those parameters were estimated approximately from the solid curves of the  $S_a-N_f$  relationship represented by a power law dependence of the applied cyclic stress and cycle number to final fracture in Figure 10. The higher ultimate tensile strength for the 7.5 mm/s samples indicates that this quantity may be more sensitive to the fatigue strength. We have reported previously<sup>[16]</sup> that excellent fatigue properties were obtained for HMC-ADC12 alloy at 1.9 mm/s, but are slightly poorer than those of the 7.5 mm/s samples, as indicated in Figure 10. On the other hand, the fatigue properties of the ADC12 alloy produced by conventional gravity casting<sup>[16]</sup> are almost the same as those of our 0.1 mm/s samples.

#### IV. DISCUSSION

As described in the previous section, the HMC samples produced at casting speeds of more than 3.5 mm/s have excellent tensile properties compared with conventional die-cast and gravity-cast samples, for example,  $\sigma_{UTS} = 246$  MPa and  $\epsilon_f = 1.7$  pct for a cold-chamber die-cast sample.<sup>[16]</sup> The lower strength and lower ductility of die-cast and gravity-cast alloys are assumed to result from internal defects and greatly enlarged microstructures. On the other hand, the high strength and high ductility of HMC samples result from very fine microstructures and uniform crystal orientation. On the basis of their microstructural characteristics, the excellent tensile properties of HMC alloys can be interpreted using the schematic diagram shown in Figure 11. Here, slip occurs in the HMC alloy at a low applied force because of the uniform crystal orientation

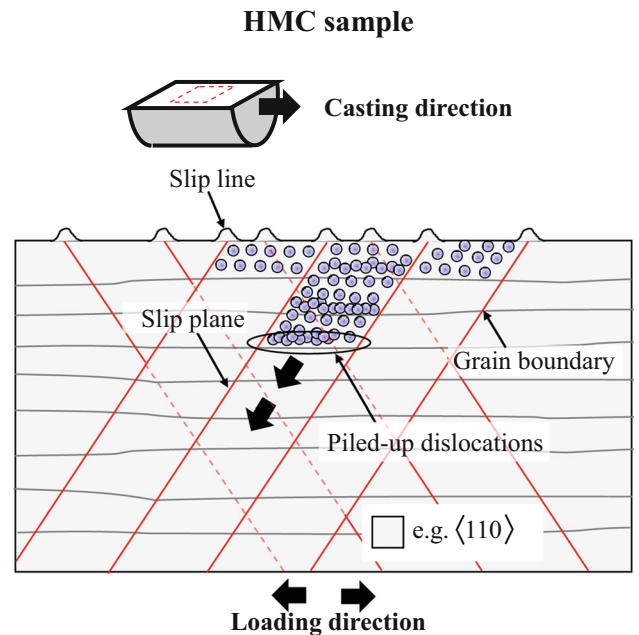


Fig. 11—Schematic illustration showing the mechanism responsible for the high strength and high ductility of HMC-ADC12 alloys.

(Figure 4(a)), leading to the high ductility; on the other hand, this slip is interrupted by thin lamellar grain boundaries (Figure 4(b)), *i.e.*, piled-up dislocations, resulting in the high strength.

As mentioned previously,  $\sigma_{UTS}$  and  $\varepsilon_f$  vary nonlinearly with casting speed (or SDAS), as shown in Figures 7(a) through (c) and 8(a) through (c). This behavior can be explained as follows: The low  $\sigma_{UTS}$  and low  $\varepsilon_f$  at low casting speeds (*e.g.*, 0.1 mm/s) result from the greatly enlarged  $\alpha$ -Al phase as well as the large brittle eutectic phases (Si and Fe based<sup>[21]</sup>). Both  $\sigma_{UTS}$  and  $\varepsilon_f$  increase with decreasing SDAS and decreasing size of the eutectic structures until the casting speed reaches approximately 3–3.5 mm/s, at which  $\sigma_{UTS} = 360$  MPa and  $\varepsilon_f = 10.5$  pct. As the casting speed increases further, the strain value decreases (*e.g.*,  $\varepsilon_f = 7.3$  pct at 7.5 mm/s), whereas the ultimate tensile strength increases because of the small SDAS, *i.e.*, grain-boundary strength ( $\sigma_{UTS} = 400$  MPa at 7.5 mm/s). In this region, the eutectic phases no longer have a strong effect on the tensile properties. From this result, it follows that the  $\alpha$ -Al phases always affect the tensile properties, whereas the eutectic phases are significant for  $\sigma_{UTS}$  and  $\varepsilon_f$  only when those phases are enlarged to more than 3  $\mu\text{m}$  (or the casting speed is less than 2.5 mm/s). These microstructural effects on tensile properties are schematically illustrated in Figure 12. Wang *et al.* have

also reported similarly that large and elongated eutectic silicon particles in cast Al alloys show the greatest tendency to crack failure.<sup>[36]</sup>

A similar approach has been followed for die-cast aluminum alloys with various silicon contents between 8.6 and 15.4 pct,<sup>[37]</sup> in which both tensile strength and fracture strain decrease dramatically with increasing silicon content. In the study by Zhang *et al.*,<sup>[26]</sup> a linear  $\sigma_{UTS}$ -SDAS relation was found for commercial A356 Al alloys, in contrast to the nonlinear relation found for our samples. They studied Al alloy samples with varying dendrite arm spacings (DASs), from about 5 to 20  $\mu\text{m}$ , which is a similar range to our samples. The different  $\sigma_{UTS}$  behavior is a consequence of the lower amount of eutectic phases in the samples studied by Zhang *et al.*,<sup>[26]</sup> which had low Si and Fe contents (6.5–7.5 and <0.2 pct, respectively). Moreover, a different trend of  $\sigma_{UTS}$  variation was found in a study of cast iron,<sup>[38]</sup> in which the ultimate tensile strength initially decreased with increasing DAS, but then showed near-plateau-like behavior for samples with DAS of more than 5  $\mu\text{m}$ . Because of the different material (cast iron vs Al alloy), a different  $\sigma_{UTS}$ -SDAS relation is to be expected. The existence of a plateau in the relation between ultimate tensile strength and DAS found in Reference 38 is due to the absence of a supercooling effect.

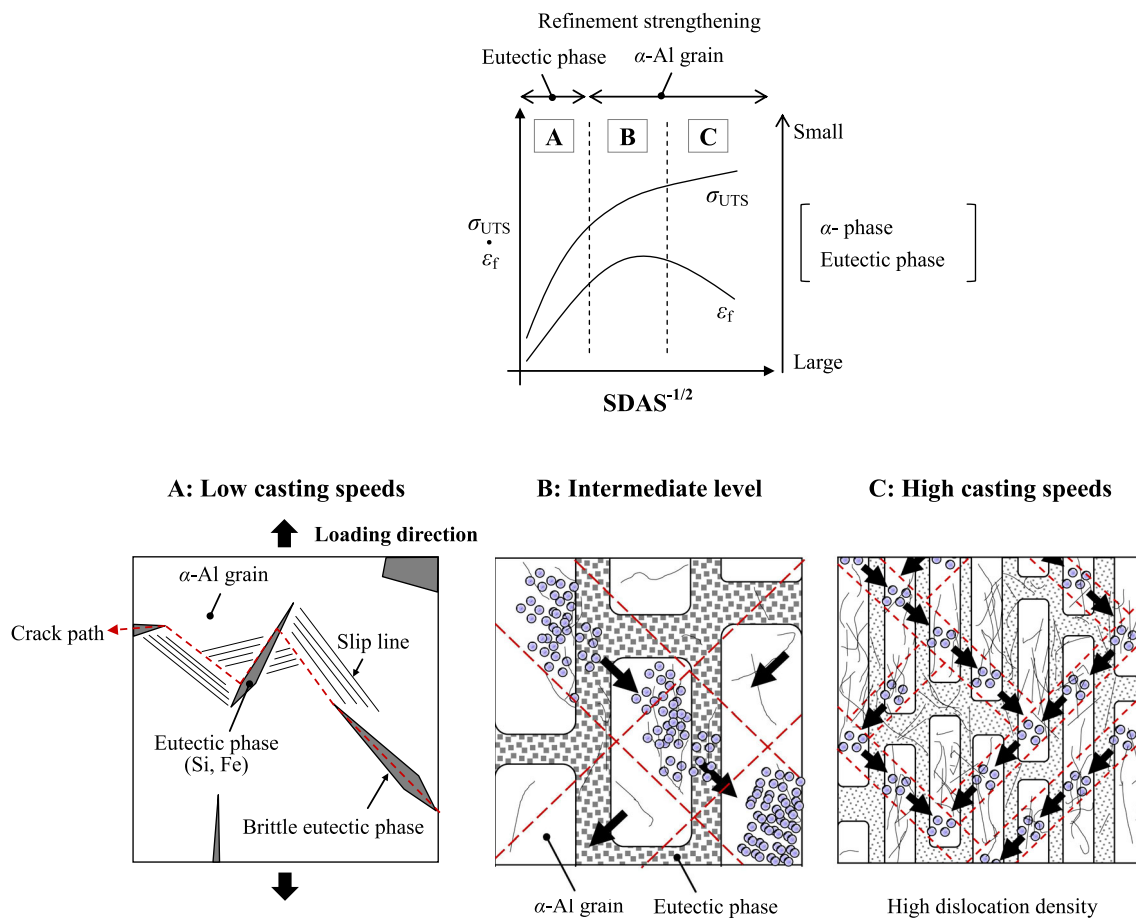


Fig. 12—Schematic diagram showing the mechanisms determining the tensile properties of cast ADC12 Al alloys.

As described in the previous section, there is a linear correlation between  $\sigma_{0.2}$  and SDAS (and thus casting speed). Our analysis suggests that the eutectic phases do not have a strong influence on the yield behavior of the cast Al alloys in this study. Furthermore, it appears that failure does not occur in the eutectic phases in samples loaded to their yield strength. To verify the failure characteristics of our samples, direct observations were made during monotonic loading. Figure 13 shows the microstructural characteristics of samples produced at casting speeds of 0.1 and 7.5 mm/s, obtained at several loading points ( $\sigma_{0.2}$ ,  $(\sigma_{UTS} + \sigma_{0.2})/2$  and  $\sigma_{UTS}$ ). There appear to be no clear material failures (microcracks) in either the eutectic phase or the  $\alpha$ -Al matrix of the 0.1 mm/s sample, even with the sample loaded to permanent deformation, for example, at  $(\sigma_{UTS} + \sigma_{0.2})/2$ . However, the density of tiny pits in the matrix and around the eutectic structures apparently increases to a value that may be taken as the dislocation density. In the sample produced at 7.5 mm/s, the specimen surfaces are severely distorted, showing meandering faces, especially between  $\alpha$ -Al grains and eutectic phases at  $\sigma_{0.2}$  and  $(\sigma_{UTS} + \sigma_{0.2})/2$ . This will be a consequence of more severe deformation of soft  $\alpha$ -Al grains and weak strain in the hard eutectic phases. On the other hand, slips and microcracks around the eutectic phases can be observed in both fractured samples, namely severe deformation does not occur until the final failure point, which is

similarly observed in the study by Wang and Cáceres.<sup>[39]</sup> Moreover, the crack initiation in both samples occurs due to the following incidents: (i) delamination-like behavior between the eutectic phase and the  $\alpha$ -Al matrix, (ii) failure in eutectic phase, and (iii) the slips in the  $\alpha$ -Al matrix. Based upon the above microstructural observation, the  $\alpha$ -Al and eutectic phases would be attributed to the tensile properties ( $\sigma_{UTS}$ ,  $\sigma_{0.2}$ , and  $\epsilon_f$ ), while weak effect of eutectic phase on the yield strength, because unclear damage in the eutectic structures is seen until just before the final fracture.

To further substantiate the failure mechanisms, an EBSD analysis was performed during monotonic loading. Figure 14 presents IPF and misorientation (MO) maps for 0.1 mm/s samples. As described in Figure 4, the IPF maps indicate the crystal orientation, which is represented by the color level in each pixel. Red solid lines in the MO maps indicate misorientation angles of more than 2 deg and less than 5 deg. From this analysis, crack initiation seems to occur from a eutectic phase as pointed by the arrow. Before crack initiation under loading, the crystal orientation around the eutectic structure seems to be altered slightly in very limited regions. However, the misorientation angle did not alter significantly from the related MO maps. In addition, even if the crack growth occurred to final failure, no clear crystal orientation change is detected in the sample. However, a slight increase in internal strain

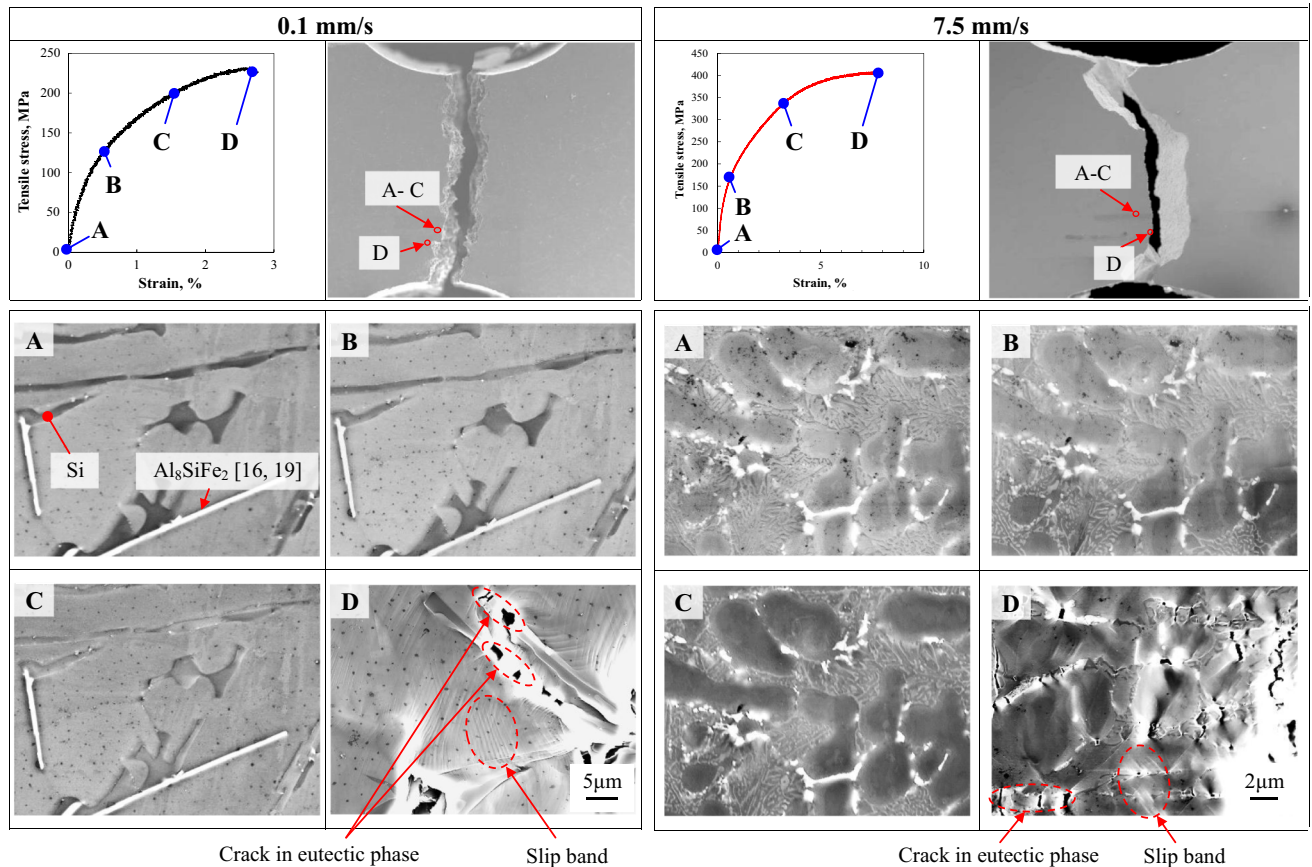


Fig. 13—SEM images showing material failure during monotonic loading to final fracture in cast ADC12 Al alloys produced at casting speeds of 0.1 and 7.5 mm/s.

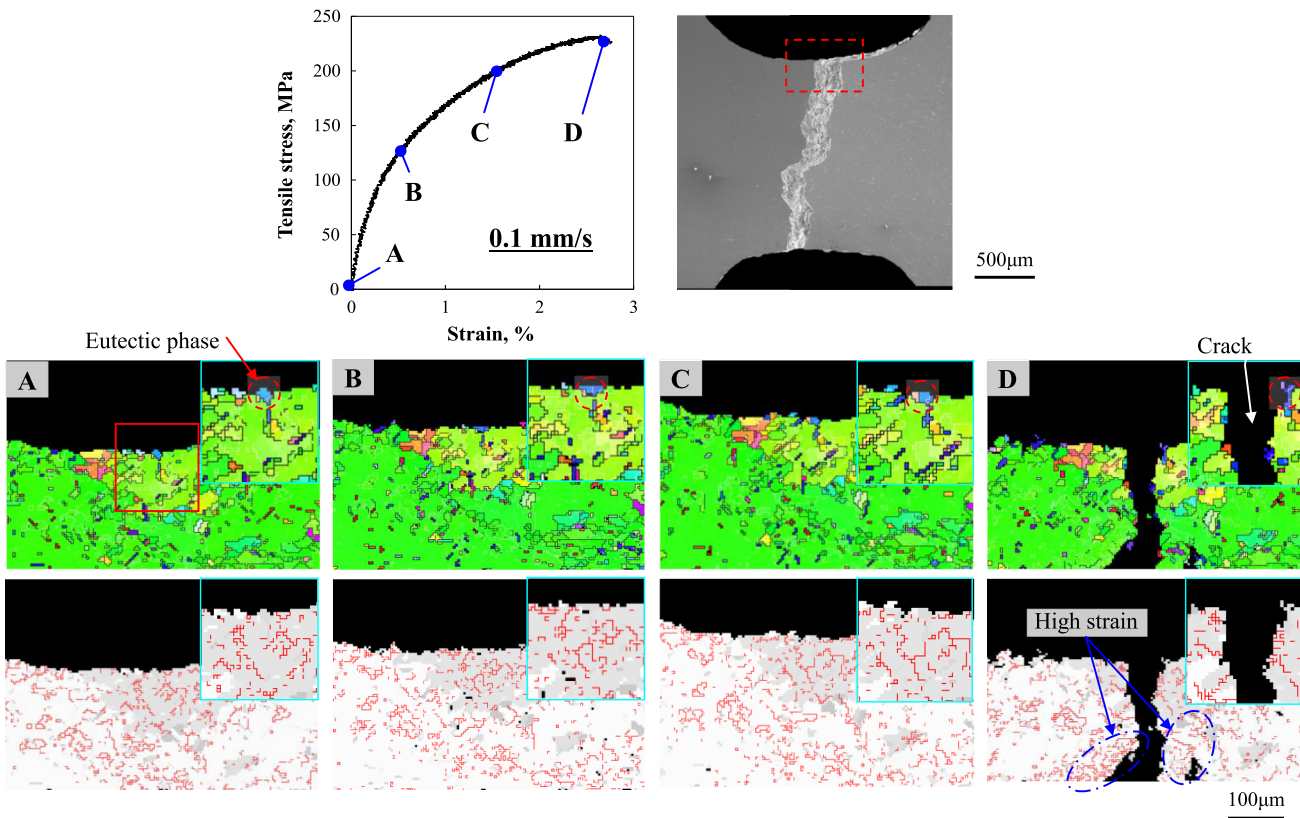


Fig. 14—EBSD analysis showing crystal orientation and misorientation angle (from 2 to 5 deg) during monotonic loading to final fracture in cast ADC12 Al alloys produced at a casting speed of 0.1 mm/s.

(a high density of the reddish zone) is detected in the MO map adjacent to the crack face, as enclosed by the dashed circles. Such a high MO angle is created by the severe strain in the final failure process.

## V. CONCLUSIONS

The effects of solidification speed on the mechanical properties of ADC12 Al alloy produced by the HMC process have been studied. On the basis of the results obtained, the following conclusions can be drawn:

1. The  $\alpha$ -Al grain size and the sizes of the eutectic structures vary with the casting speed because of the different solidification rates at different speeds. A relatively uniform crystal orientation is obtained, even if the casting speed varies. The microstructure ( $\alpha$ -Al grains) grows clearly in the casting direction. Even though the sizes of microstructures vary, no differences in crystal orientation and no clear cast defects are detected at different casting speeds.
2. There are clear correlations between tensile strength and microstructural characteristics (SDAS), with tensile strengths  $\sigma_{UTS}$  increasing nonlinearly with decreasing SDAS. A linear correlation between  $\sigma_{0.2}$  and SDAS. A convex shape of fracture strain  $\epsilon_f$  vs SDAS is detected. Such different trends are attributed to the size of the eutectic phases. The yield behavior is not affected strongly by the eutectic

structures, since failure in the eutectic phases occurs just before final fracture. Although the size of eutectic phases is decreased to tiny size of a few microns with the increasing cooling rate, such tiny eutectic phase cannot be further changed even if the cooling rate increases. Unlike eutectic structures, the SDAS is decreased further with increasing the cooling rate. Those microstructural characteristics make the nonlinear  $\sigma_{UTS}$  vs SDAS and concave  $\epsilon_f$  vs SDAS.

3. Fracture models have been proposed and illustrated schematically. The high strength and high ductility of the HMC samples result from the existence of very fine microstructures and the uniform crystal orientation: dislocation movement is facilitated by the uniform crystal orientation, leading to the high ductility, but this slip is interrupted by thin lamellar grain boundaries (piled-up dislocations), resulting in the high strength.

## ACKNOWLEDGMENTS

This work was supported by a grant (Grant-in-Aid for Scientific Research (C), 2014) from the Japanese Government (Ministry of Education, Science, Sports and Culture) and the Light Metal Educational Foundation Inc.

## REFERENCES

1. A. Inoue, T. Nakamura, N. Nishiyama, and T. Masumoto: *Mater. Trans. JIM*, 1992, vol. 33, pp. 937–45.
2. O. Kuwazuru, Y. Murata, Y. Hangai, T. Utsunomiya, S. Kitahara, and N. Yoshikawa: *J. Solid Mech. Mater. Eng.*, 2008, vol. 2, pp. 1220–31.
3. A.K.M. Aziz Ahamed and H. Kato: *Mater. Trans. JIM*, 2008, vol. 49, pp. 1621–28.
4. H.D. Zhao, F. Wang, Y.Y. Li, and W. Xia: *J. Mater. Process. Technol.*, 2009, vol. 209, pp. 4537–42.
5. S. Jana, R.S. Mishra, J.B. Baumann, and G. Grant: *Acta Mater.*, 2010, vol. 58, pp. 989–93.
6. M.S. Kabir, E.A. Ashrafi, T.I. Minhaj, and M.M. Islam: *Int. J. Eng. Adv. Technol.*, 2014, vol. 3, pp. 115–20.
7. K.M. Youssef, R.O. Scattergood, K.L. Murty, and C.C. Koch: *Scripta Mater.*, 2006, vol. 54, pp. 251–56.
8. Z. Horita, T. Fujinami, M. Nemoto, and T.G. Langdon: *Metall. Mater. Trans. A*, 2000, vol. 31A, pp. 691–701.
9. C.E. Carlton and P.J. Ferreira: *Acta Mater.*, 2007, vol. 55, pp. 3749–56.
10. Q.G. Wang, D. Apelian, and D.A. Lados: *J. Light Met.*, 2001, vol. 1, pp. 85–97.
11. M. Kobayashi, H. Hara, H. Toda, D. Sugiyama, and N. Kuroda: *Int. J. Cast Met. Res.*, 2012, vol. 25, pp. 31–37.
12. Q.G. Wang: *Metall. Mater. Trans. A*, 2003, vol. 34A, pp. 2887–99.
13. Q.G. Wang: *Metall. Mater. Trans. A*, 2004, vol. 35A, pp. 2707–18.
14. M.A. Irfan, D. Schwam, A. Karve, and R. Ryder: *Mater. Sci. Eng. A*, 2012, vol. 535, pp. 108–14.
15. S. Sengupta, H. Soda, and A. Mclean: *J. Mater. Sci.*, 2002, vol. 37, pp. 1747–58.
16. M. Okayasu, K. Ota, S. Takeuchi, H. Ohfuji, and T. Shiraishi: *Mater. Sci. Eng. A*, 2014, vol. 592, pp. 189–200.
17. A. Ohno: *Solidification*, Springer, Berlin, 1987, pp. 113–18.
18. M. Okayasu, Y. Ohkura, S. Takeuchi, S. Takasu, H. Ohfuji, and T. Shiraishi: *Mater. Sci. Eng. A*, 2012, vol. 543, pp. 185–92.
19. H. Xin and Y. Hong: *J. Wuhan Univ. Tech.-Mater. Sci. Ed.*, 2013, vol. 28, pp. 202–05.
20. M. Vandyoussefi and A.L. Greer: *Acta Mater.*, 2002, vol. 50, pp. 1693–03.
21. M. Okayasu, S. Takasu, and M. Mizuno: *J. Mater. Sci.*, 2012, vol. 47, pp. 241–50.
22. X. Hu, F. Jiang, F. Ai, and H. Yan: *J. Alloy. Compd.*, 2012, vol. 538, pp. 21–27.
23. R.N. Lumley, N. Deeva, R. Larsen, J. Gembarovic, and J. Freeman: *Metall. Mater. Trans. A*, 2013, vol. 44A, pp. 1074–86.
24. Y. Kawaguchi, M. Sugamata, and J. Kaneko: *J. Jpn. Inst. Light Met.*, 1997, vol. 47, pp. 3–9 (Japanese).
25. L. Ceschini, A. Morri, A. Morri, A. Gamberini, and S. Messieri: *Mater. Des.*, 2009, vol. 30, pp. 4525–31.
26. L.Y. Zhang, Y.H. Jiang, Z. Ma, S.F. Shan, Y.Z. Jia, C.Z. Fan, and W.K. Wang: *J. Mater. Process. Technol.*, 2008, vol. 207, pp. 107–11.
27. G. Ran, J. Zhou, and Q.G. Wang: *J. Alloy. Compd.*, 2006, vol. 421, pp. 80–86.
28. A.A. Benzerga, S.S. Hong, K.S. Kim, A. Needleman, and E.V.D. Giessen: *Acta Mater.*, 2001, vol. 49, pp. 3071–83.
29. Q.G. Wang, M. Praud, A. Needleman, K.S. Kim, J.R. Griffiths, C.J. Davidson, C.H. Cáceres, and A.A. Benzerga: *Acta Mater.*, 2010, vol. 58, pp. 3006–13.
30. I. Kovács, J. Lendvai, T. Ungár, G. Groma, and J. Lakner: *Acta Metall.*, 1980, vol. 28, pp. 1621–31.
31. M. Tiryakioglu, J. Campbell, and N.D. Alexopoulos: *Metall. Mater. Trans. A*, 2009, vol. 40A, pp. 1000–1007.
32. D.G. Eskin and L. Suyitno: *Prog. Mater. Sci.*, 2004, vol. 49, pp. 629–11.
33. I. Brooks, P. Lin, G. Palumbo, G.D. Hibbard, and U. Erb: *Mater. Sci. Eng. A*, 2008, vol. 491, pp. 412–19.
34. Y.-L. Shen and N. Chawla: *Mater. Sci. Eng. A*, 2001, vol. 297, pp. 44–47.
35. J.R. Cahoon, W.H. Broughton, and A.R. Kutzak: *Metall. Trans.*, 1971, vol. 2, pp. 1979–83.
36. Q.G. Wang, C.H. Cáceres, and J.R. Griffiths: *Metall. Mater. Trans. A*, 2003, vol. 34A, pp. 2901–12.
37. M. Okayasu, N. Nishi, and K. Kanazawa: *J. Jpn. Foundry Eng. Soc.*, 1998, vol. 70, pp. 266–72.
38. K.H.W. Seah, J. Hemanth, and S.C. Sharma: *J. Mater. Sci.*, 1998, vol. 33, pp. 23–28.
39. Q.G. Wang and C.H. Cáceres: *Mater. Sci. Eng. A*, 1998, vol. 241, pp. 72–82.